https://doi.org/10.5194/egusphere-2026-844
Preprint. Discussion started: 16 April 2026

1.645 µm differential absorption lidar measurements of atmospheric methane using an Er:YAG laser

Dimitri Edouart, Fabien Gibert, Claire Cénac

Laboratoire de Météorologie Dynamique (LMD/IPSL), École polytechnique, Institut polytechnique de Paris, Sorbonne Université, École normale supérieure, PSL Research University, CNRS, École des Ponts, Palaiseau, France

Correspondence to: Dimitri Edouart (dimitri.edouart@lmd.ipsl.fr)

Abstract. A differential absorption lidar (DIAL) based on an Er:YAG laser was used to retrieve methane concentration profiles within the mixed layer along a near-horizontal line of sight (4° above the horizontal) from the École Polytechnique site, directed northward toward the western part of the city of Paris. The achieved precision remains below 1% up to a range of 3.5 km for profiles with a spatio-temporal resolution of 470 m / 20 min. The measurements were compared with in situ observations from an ICOS site located 5 km from the lidar. The lidar successfully captured the late stage of the dispersion of a methane plume originating from a fire occurred at a waste-sorting facility in the city of Paris, in good agreement with the in situ measurements. Both random and systematic errors in the lidar measurements are dominated by uncertainties in the ON wavelength measurement.

1 Introduction

Methane (CH_4) is the second most important anthropogenic greenhouse gas after CO_2. CH_4 emissions come from various sources, ~ 60% of which being anthropogenic through three major processes: anaerobic biochemical degradation of organic matter (wetlands, termites, livestock, rice cultivation, landfills); natural degassing of the Earth's crust and the exploitation of fossil fuels; and biomass burning under low-oxygen conditions (Saunois et al. 2020). The terrestrial sink of CH_4 results primarily (~90%) from oxidation by the OH radical and from chemical reactions with the Cl radical (in the marine environment) or from heterogeneous reactions (in dry soils). The current trend, i.e., the significant increase of atmospheric CH_4 since 2007, is not compatible with the Paris Agreement's objective of limiting the global warming to below 2°C compared to pre-industrial levels and requires action from the scientific community to understand, locate, measure, and verify inventories of CH_4 emissions across various spatial scales. An in-situ measurement network exists at the surface (150 stations) but remains heterogenous in time and space, while uncertainties concern both individual processes and the regional scale. These observations are completed by vertical profiles in the troposphere (routine AIRCORE profiles) (Membrive et al. 2017), by passive remote sensing measurements from the ground (TCCON) (Zhou et al. 2019), and, since 2003, by reconstructions of integrated methane columns from space (SCIAMACHY, IASI, TANSO-FTS (GOSAT), TROPOMI) (Buchwitz et al. 2000; Clerbaux et al. 1998; Butz et al. 2011; Lorente et al. 2021 among others). Private nanosats (e.g., GHGsat, Bluefield, methaneSAT) also have objectives for estimating local industrial sources.

Differential absorption lidar (DIAL) is well suited tool to monitor CH_4 concentration in the atmosphere, as it enables three-dimensional mapping of anthropogenic methane plumes, vertical profiling in the troposphere and study of the atmospheric transport when combined with wind measurements. Note that global observations from space are also foreseen in a near future with the development of the MERLIN CH_4 lidar mission (launch is currently planned to 2029) (Ehret et al. 2017).

Since the late 1990s, several DIAL systems have been developed for atmospheric methane measurements. Ikuta et al. (1999) used a Ti:sapphire laser combined with a Raman cell to access methane absorption lines near 1.67 µm, with a system primarily dedicated to methane leak detection at ranges of a few hundred meters. The National Physical Laboratory (NPL, UK) subsequently developed a containerized DIAL system with scanning capabilities for field deployments, dedicated to monitoring methane emissions at industrial sites (Innocenti et al., 2017). ONERA also developed a DIAL system for industrial

https://doi.org/10.5194/egusphere-2026-844
Preprint. Discussion started: 16 April 2026

methane leak detection (Cézard et al., 2020), based on fiber laser technology combined with a Raman cell to reach methane absorption lines. Its heterodyne detection scheme additionally enables radial wind measurements, opening perspectives for the quantification of methane emission rates. Stroud et al. (2023) developed a multi-wavelength DIAL system based on an optical parametric oscillator (OPO) laser and photomultiplier tube (PMT) detection. The multi-wavelength capability relaxes the constraints on wavelength accuracy. The airborne HALO (High Altitude Lidar Observatory) system, also based on an OPO laser and using InGaAs avalanche photodiode (APD) detection, is primarily dedicated to integrated path differential absorption (IPDA) measurements, but has demonstrated its capability to retrieve methane profiles within the atmospheric boundary layer (Barton et al., 2022). Meng et al. (2018) proposed an alternative detection approach using nonlinear optical frequency conversion (upconversion detection), enabling the use of PMTs in the visible spectral range, where detector performance is significantly enhanced, and demonstrating promising potential for range-resolved methane measurements. Veselovskii et al. (2019) investigated the retrieval of atmospheric methane profiles using the Raman lidar technique. Due to the very weak Raman signal, measurements are limited to nighttime conditions, and significant biases were reported, potentially originating from aerosol fluorescence.

In this study, we present methane mixing ratio profile measurements obtained with a DIAL system using a novel laser source based on Er:YAG crystals (Edouart et al., 2024). This laser technology provides high optical power with good wall-plug efficiency and features a simpler architecture compared to OPO-based systems. We first describe the lidar system design, then detail the data processing chain used to retrieve methane mixing ratio profiles. Atmospheric measurements performed along a quasi-horizontal line of sight and their comparison with in situ observations are presented. Finally, the main sources of random and systematic errors affecting the lidar measurements are identified and quantified.

2 DIAL set-up

The schematic layout of the lidar system is shown in Figure 1 and its main specifications are summarized in Table 1. The laser source is a prototype developed in the laboratory. Its operation and performance have been described in detail in Edouart et al. 2024. Here, we briefly recall its main characteristics. The laser cavity contains an 8-cm long Er:YAG rod (0.25% doping) and an acousto-optic Q-switch (AOM) enabling pulsed operation. The output coupler transmission is 20%. The dichroic mirrors surrounding the Er:YAG crystal are plane, while those around the AOM Q-switch are concave with a radius of curvature of 1 m. Two linearly polarized Erbium-doped fiber pump lasers (IPG Photonics—model ELR-30-1532-LP), each delivering 30 W at 1532 nm, are combined using a polarizer to end pump the Er:YAG crystal inside the cavity. An additional polarizer is inserted in the cavity to enforce linearly polarized emission. Although such polarization is not required for direct-detection DIAL measurements, it enables the future implementation of a heterodyne detection channel, thus allowing simultaneous wind velocity retrieval in addition to methane concentration measurements as it was previously done for CO_2 (Gibert et al. 2015). Provided that the spatio-temporal resolution is sufficient, this combination could give access to turbulent methane flux measurements using the lidar eddy-covariance technique (Gibert et al. 2025). The laser cavity is seeded alternately by two continuous-wave (CW) fiber-coupled distributed-feedback (DFB) diode lasers (output power: 15 mW), using a fast fiber switch (fSWT). The seeders are injected into the laser cavity through the first diffraction order of the AOM. A booster optical amplifier (BOA) is employed to maintain an injection power of 15 mW despite insertion losses of the fiber components. One DFB wavelength is tuned to the center of the methane triplet at 1645.55 nm (ON line), while the second is tuned close to the absorption line at 1645.39 nm (OFF line). Each wavelength is locked to the cavity resonance by applying an external phase modulation with an electro-optic modulator (EOM) and implementing a Pound-Drever-Hall (PDH) double-phase servo loop (Gibert et al., 2014). Despite the difference in Er:YAG gain between the ON and OFF wavelengths, the laser emits pulses with identical energy (7 mJ) and duration (300 ns) at a repetition rate of 1 kHz, as a differential loss is introduced by the AOM Q-

https://doi.org/10.5194/egusphere-2026-844
Preprint. Discussion started: 16 April 2026

switch between the two wavelengths (Edouart et al. 2024). Two fiber couplers extract 10% of the power from each DFB for wavelength monitoring with a wavemeter (Bristol 621 A-IR, accuracy: 35 MHz @ 1645 nm). The wavelength measurement alternates between the two DFBs using a fiber switch (sSWT) toggling every 10 s, thereby tracking the slow drift of each seeder locked to the laser cavity. A beam expander with a magnification of ×8 is used to reduce the laser beam divergence to approximately 300 µrad (full angle). Relay mirrors direct the beam vertically along the telescope optical axis. A large gold-coated steering mirror is used to direct the beam along a nearly horizontal line-of-sight while reflecting the atmospheric backscattered lidar signal towards the telescope. An elevation angle of 4° above the horizontal was maintained to avoid obstacles in the line-of-sight. The telescope is of Newtonian type, with a 50-cm diameter primary mirror (gold-coated) and a focal length of 1.65 m. An iris placed at the focal plane limits the detection field-of-view (full angle) to 600 µrad. An interference filter centered at 1645.55 nm with a 1-nm bandwidth is used to filter the solar background while transmitting the laser wavelengths. The telescope primary mirror is imaged onto the photocathode of a photomultiplier tube (NIR PMT, Hamamatsu-H10330C-75), and the signal is subsequently digitized by a lidar signal acquisition module (Licel TR80-16bit-3U). The PMT gain is limited to 3 10^5 (corresponding to an applied voltage of –400 V) in order to restrict the continuous anode current generated by the solar background transmitted through the interference filter during daytime measurements. The Licel acquisition module can operate in both the analog mode (voltage digitization via an analog-to-digital converter) and the photon-counting mode. The measurements presented here make use of the analog mode only. It should be noted that, since the laser pulse duration is 300 ns, the spatial resolution of the lidar profile cannot exceed 45 m. As the lidar signal is sampled at 80 MSamples/s by the acquisition module, corresponding to one point every 1.9 m, the profile is therefore oversampled with respect to its actual spatial resolution.

The lidar system is installed on the second floor of the laboratory, located 10 km southwest of Paris. The 45° steering mirror positioned above the telescope is mounted at roof level, approximately 15 m above ground. The laser beam is directed northward, toward the western suburbs of Paris.

https://doi.org/10.5194/egusphere-2026-844
Preprint. Discussion started: 16 April 2026

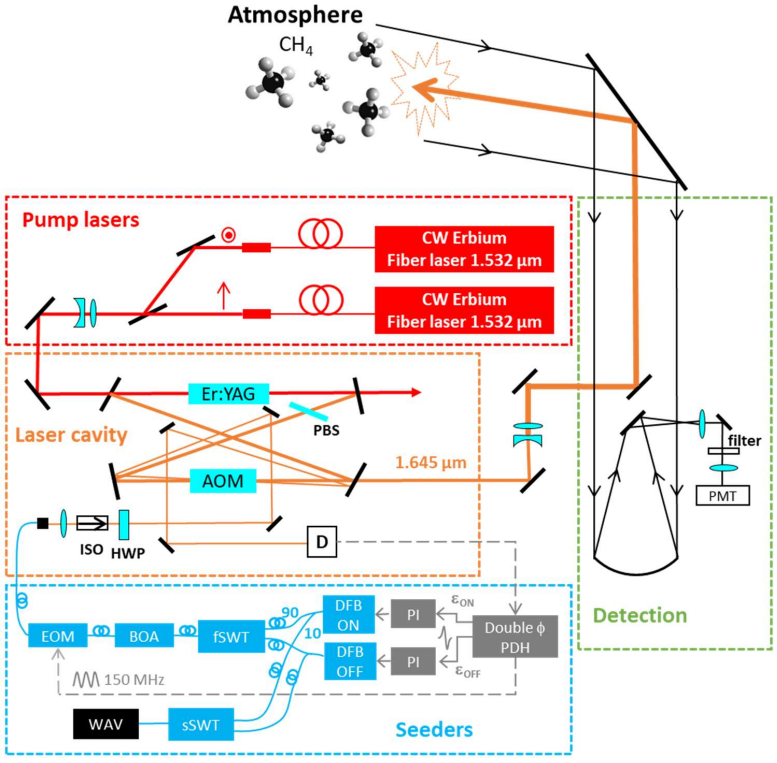

Figure 1: DIAL set-up for methane measurements. AOM: acousto-optic modulator, PBS: polarization beam splitter, ISO: optical isolator, HWP: half wave plate, D: detector, EOM: electro optic modulator, BOA: boost optical amplifier, fSWT: fast optical switch, sSWT: slow optical switch, WAV: wavemeter, PI: proportional integral servo controller, PMT: photo-multiplier tube

Table 1: Main specifications of the methane DIAL

Transmitter		**Receiver**	
Pulse energy	7 mJ	Telescope Field of view	Diameter 50 cm / focal length 1.65 m 600 µrad (full angle)
Pulse duration	300 ns	LOS elevation	4°
PRF	1 kHz (DIAL: 500 Hz)	Filter	Transmission: 0.8 @ 1645.55 nm, bandwidth : 1 nm,
Wavelengths	OFF 1645.39 nm ON 1645.55 nm	Detector	NIR PMT, quantum efficiency : 1.1 % @1645 nm, Gain : 3 10^5
divergence	300 µrad (with x8 magnification)	Data acquisition system	Licel TR80, bandwidth: 40 MHz, sampling rate: 80 MS/s, precision:16 bit

3 Data processing

3.1 DIAL equations

The principle of the DIAL (Differential Absorption Lidar) technique for measuring atmospheric methane profiles relies on the acquisition of two lidar signals. The first one, referred to as the OFF-line profile, corresponds to a wavelength only weakly absorbed by the atmospheric gases, particularly methane, and serves as a reference. The second one, the ON-line profile, is spectrally positioned on a methane absorption line that is spectrally isolated from the absorption lines of other atmospheric

https://doi.org/10.5194/egusphere-2026-844
Preprint. Discussion started: 16 April 2026

constituents and as close as possible in wavelength to the OFF-line. Consequently, the only significant difference between the two profiles arises from methane absorption. From these two profiles, the differential absorption optical depth (DAOD) due to methane absorption along the line of sight can be computed and related to the methane dry-air mixing ratio profile by the following expression:

$$DAOD(R) = \frac{1}{2} ln\left(\frac{S(\lambda_{OFF},R)}{S(\lambda_{ON},R)}\right) = \int_0^R X_{CH_4}(r) n_d(r) \left[\tilde{\sigma}_{CH_4}(\lambda_{ON},r) - \tilde{\sigma}_{CH_4}(\lambda_{OFF},r)\right] dr \quad (1)$$

where $S(\lambda_{OFF},R)$, $S(\lambda_{ON},R)$ are the lidar power profiles at the OFF and ON wavelengths, respectively; $X_{CH_4}(r)$ is the methane dry-air mixing ratio profile; $n_d(r)$ is the dry-air molecular number density profile; and $\tilde{\sigma}_{CH_4}(\lambda_{ON},r)$, $\tilde{\sigma}_{CH_4}(\lambda_{OFF},r)$ are the effective methane absorption cross-sections at the ON and OFF wavelengths. The methane mixing ratio profile is then retrieved by derivation of the previous expression:

$$X_{CH_4}(R) = \frac{\alpha(R)}{WF(R)} \quad (2)$$

with $\alpha(R) = \frac{dDAOD(R)}{dR}$, the differential absorption coefficient, and $WF(R) = n_d(R)\left[\tilde{\sigma}_{CH_4}(\lambda_{ON},R) - \tilde{\sigma}_{CH_4}(\lambda_{OFF},R)\right]$, the weighting function.

The ON and OFF lidar profiles used to compute the differential optical depth are averaged over several laser shots and spatially integrated along the line of sight, resulting in a coarser effective range resolution than the original sampling resolution of 1.9 m at 80 MS/s. Such spatial and temporal averaging is necessary to achieve sufficient signal-to-noise ratios (SNR), ensuring that the ratio remains positive and that the optical depth (Eq. (1)) can be reliably computed. The ratio of the two profiles can then be temporally integrated so that the SNR on the optical depth becomes high enough to allow a bias-minimized estimation of its derivative. These considerations regarding the space and time integration of the lidar profiles will be discussed in more detail in a subsequent section.

3.2 Weighting function calculation and spectroscopy

To retrieve the methane mixing ratio profile, the DIAL method requires the computation of the weighting function. The effective absorption cross-sections $\tilde{\sigma}_{CH_4}$ take into account the laser spectral linewidth and possible spectral impurities of the emitted pulses. In the present measurements, which are limited to the atmospheric boundary layer, the lidar backscatter is dominated by Mie scattering from aerosols. This scattering regime causes a spectral broadening of the scattered light on the order of a few MHz, which remains negligible compared with the methane absorption linewidths (typically of the order of GHz). Furthermore, the spectral impurity of the laser source used here can also be neglected (Edouart et al., 2024). As a result, the effective absorption cross-sections can be considered equal to the methane absorption cross-sections at the ON and OFF wavelengths and the weighting function can thus be expressed as:

$$WF(R) = n_d(R)\left[\sigma_{CH_4}(\lambda_{ON},R) - \sigma_{CH_4}(\lambda_{OFF},R)\right] \quad (3)$$

The dry-air number density profile is given by:

$$n_d(R) = \frac{p(R)}{k_B T(R)} \frac{1}{1+\rho_w(R)} \quad (4)$$

where p, T, ρ_w are the pressure, temperature, and water vapor mixing ratio profiles along the line of sight, and k_B is the Boltzmann constant. In addition, the absorption cross sections also depend on temperature and pressure. Consequently, computing the weighting function requires knowledge of the pressure, temperature, and water vapor profiles. For the quasi-horizontal profiles considered here, standard atmospheric profiles are assumed.

The methane absorption cross-sections are obtained by interpolating precomputed spectral atlases with a resolution of 5 10^{-4} cm^{-1}, covering the range of thermodynamic conditions encountered in the atmosphere (44 pressure levels and 12 temperature levels per pressure level). These atlases are generated using the HITRAN2020 spectroscopic database (Gordon et al. 2022), which includes recent improvements in methane spectroscopic parameters (Delahaye et al. 2016, 2019). The calculations apply

https://doi.org/10.5194/egusphere-2026-844
Preprint. Discussion started: 16 April 2026

the Hartmann–Tran line-shape model (Ngo et al. 2013) and account for line mixing, particularly for the methane multiplet near the ON wavelength. Figure 2 shows the absorption spectra of methane, water vapor, and carbon dioxide at ground level. The CO_2 lines can be neglected, whereas water vapor contributes non-negligibly to the total absorption, especially between 1645.0–1645.5 nm and beyond 1645.7 nm. Because water vapor concentration can vary by more than an order of magnitude, it is essential to select ON and OFF wavelengths with similar water vapor absorption. Three OFF candidates were considered: 1645.31 nm, 1645.39 nm, and 1645.88 nm. Due to the Er:YAG gain bandwidth, wavelengths beyond 1645.6 nm are difficult to reach (Edouart et al., 2024). Although using 1645.31 nm as the OFF wavelength would provide a slightly larger differential optical depth, this wavelength lies near the edge of the interference filter transmission band. Therefore, 1645.39 nm was selected as the OFF wavelength. In the current laser configuration, the ON and OFF wavelengths may slightly drift over time, since they are locked to the laser cavity rather than to an absolute reference (e.g., a methane absorption cell). As the wavelengths are continuously monitored by the wavemeter, the weighting function can be recalculated accordingly to compensate for these drifts. However, such drifts may also lead to incomplete compensation of residual water vapor absorption between the ON and OFF wavelengths. In that case, the contribution of water vapor must be subtracted from the measured differential absorption coefficient prior to deriving the methane mixing ratio profile, using either external water vapor measurements or a modeled humidity profile.

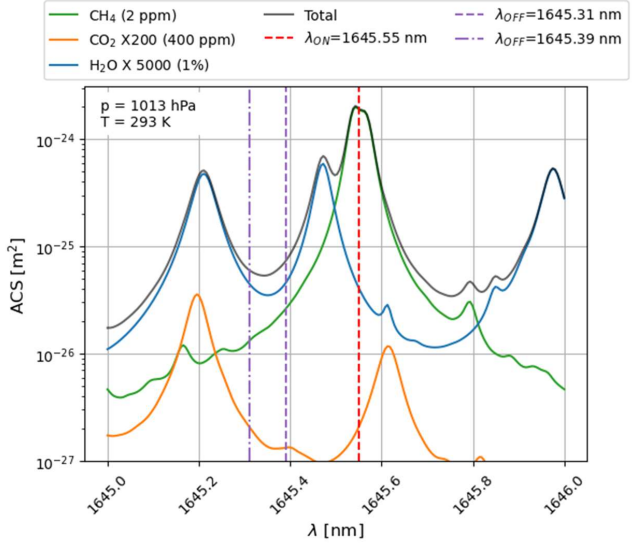

Figure 2: Absorption cross sections of the CH_4 multiplet near 1645.55 nm, together with those of H_2O and CO_2 normalized to their relative atmospheric abundances with respect to CH_4. The positions of the ON wavelength and the OFF wavelengths accessible with the Er:YAG laser are also indicated.

3 Atmospheric measurements

3.1 ON and OFF lidar profiles

The lidar measurements were conducted on the morning of 8 April 2025 between 10:30 and 13:30 local time. The Licel acquisition module integrates 2000 laser shots for both ON and OFF wavelengths in real time, resulting in ON and OFF profiles recorded with a temporal resolution of 4 s. A screening of the profiles is performed to eliminate those obtained with improperly seeded laser pulses, which are likely to exhibit a non-compliant spectral profile. This screening is carried out by monitoring

https://doi.org/10.5194/egusphere-2026-844
Preprint. Discussion started: 16 April 2026

the pulse build-up time. Under nominal operating conditions (i.e., in the absence of significant mechanical or thermal disturbances), such malfunctions are rare (<0.3%). These raw ON and OFF profiles are then integrated along the line of sight using a 25-point moving average. The resulting spatial resolution is therefore 47 m, which corresponds to the limit imposed by the 300-ns laser pulse duration. Distance-corrected ON and OFF quicklook profiles are shown in Figure 3 (left). The color scale is displayed on a logarithmic axis because the signal dynamics between particulate and molecular scattering are very large in the near-infrared. At the beginning of the measurement sequence, since the laser beam is slightly inclined upward (4° above horizontal), it exits the boundary layer at a distance of 4 km. The subsequent rise of the boundary layer over the course of the time series is clearly observable. The retrieval of methane mixing ratios will here be limited to the first 5 kilometers, where atmospheric backscatter is dominated by particulate scattering. Indeed, because molecular scattering in the near-infrared is much weaker than particulate scattering, the measurement precision degrades significantly outside the boundary layer. Moreover, DIAL processing using signals dominated by molecular scattering is more complex (Bosenberg 1998) and will be addressed in a subsequent publication.

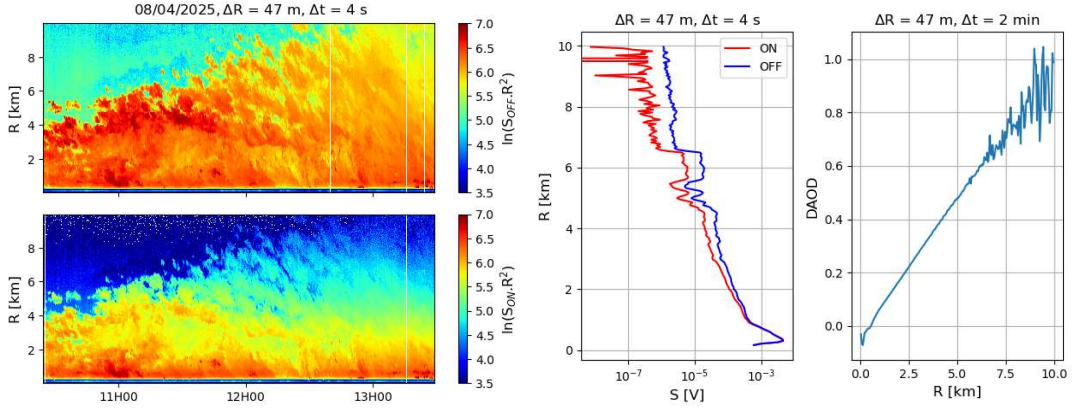

Figure 3: (left) Time series of the logarithm of the range-squared-corrected ON and OFF signals. (right) Examples of ON and OFF signals and the corresponding DAOD around 11H16.

3.2 Temporal integration of the lidar signals

To determine the minimum temporal integration times for the ON and OFF signals, Figure 4 (left) presents the Allan deviations of these signals at distances of 5 km and 10 km. For the ON and OFF signals at 5 km, the Allan deviation follows a $\tau^{1/3}$ dependence up to $\tau \approx 100$ s. This indicates that the signal fluctuations are dominated by turbulent atmospheric motions following a Kolmogorov law. The instrumental noise of the 4-s integrated signals is therefore lower than the atmospheric turbulent fluctuations. At a distance of 10 km, the ON-signal fluctuations are dominated by white instrumental noise ($(\tau^{-1/2}$ law) up to $\tau \approx 30$ s. Thus, at this range, additional temporal averaging of the lidar signals is required to reduce instrumental noise before atmospheric fluctuations can emerge. The OFF-signal fluctuations at 10 km lie between both regimes at small τ and then follow a Kolmogorov-type behavior similar to the 5-km signals. For $\tau > 100$ s, turbulent fluctuations give way to larger-scale atmospheric variations.

https://doi.org/10.5194/egusphere-2026-844
Preprint. Discussion started: 16 April 2026

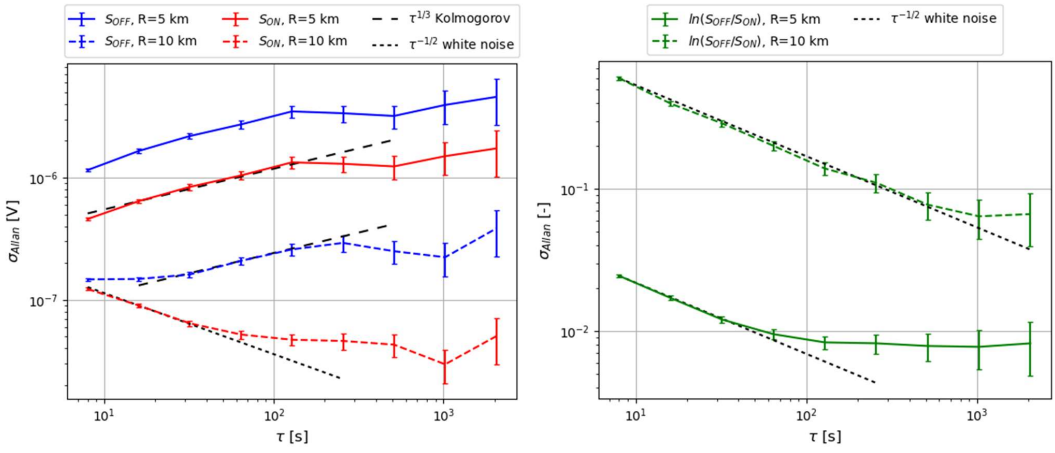

Figure 4: (Left) Allan deviation of the ON and OFF signals at ranges of 5 and 10 km. (Right) Allan deviation of the DAOD at 5 and 10 km. Characteristic Allan deviation trends for white noise and for a turbulent signal with a Kolmogorov-type spectrum are added for comparison.

When the temporal integration of the lidar signals is sufficient for instrumental noise to become negligible, the DAOD can be retrieved. Turbulent fluctuations in the ON and OFF signals cancel in the ratio S_{OFF}/S_{ON}, leaving the DAOD dominated by instrumental noise. This is illustrated in Figure 4 (right), which shows the Allan deviation of $ln(S_{OFF}/S_{ON})$ at distances of 5 km and 10 km. At 5 km, white instrumental noise dominates the DAOD fluctuations for τ up to roughly 100 s. This indicates that after a few minutes of integration, the lidar precision is sufficient to resolve fluctuations in atmospheric methane concentration and/or a drift of the weighting function. Such a potential drift of the weighting function may in particular be caused by spectral drifts of the laser wavelength, which is not actively stabilized. At a distance of 10 km, the DAOD must be averaged for more than one thousand seconds (~17 min) for instrumental noise to become negligible. Accordingly, for ranges shorter than 5 km, the DAOD will be integrated over 2 minutes in order to minimize instrumental white noise. Figure 3 (right) shows an example of the DAOD integrated over 2 minutes. Further integration of the DAOD could introduce an additional error in the retrieval of the methane mixing ratio due to a potential drift of the weighting function. To further reduce the statistical uncertainty, the methane mixing ratio itself must then be temporally averaged. In this study, methane mixing ratios retrieved with a 2-minute temporal resolution are averaged over 20 minutes to reduce the statistical error.

3.2 Calculation of the weighting function

To compute the weighting function (see Eq. (3)), it is first necessary to determine the dry air density profile (see Eq. (4)). The SIRTA observatory at the École Polytechnique site (https://sirta.ipsl.fr/) provides measurements of surface pressure, as well as temperature and humidity measured on a 50-m mast. Since the laser beam has a slight upward inclination (4° above the horizontal), typical decreases in temperature and pressure with altitude are taken into account in the calculation of the weighting function. The water vapor mixing ratio is assumed to be constant, as the lidar measurement of the methane profile is restricted to the mixed layer. The temperature and pressure profiles are also used to compute the absorption cross sections by interpolating spectroscopic atlases at the ON and OFF wavelengths recorded by the wavemeter. Figure 5 shows the time series of surface pressure, temperature, and humidity, as well as the wavelength drifts of the ON and OFF pulses and the corresponding weighting functions at the lidar location (R=0 km) and at a range R=5 km.

https://doi.org/10.5194/egusphere-2026-844
Preprint. Discussion started: 16 April 2026

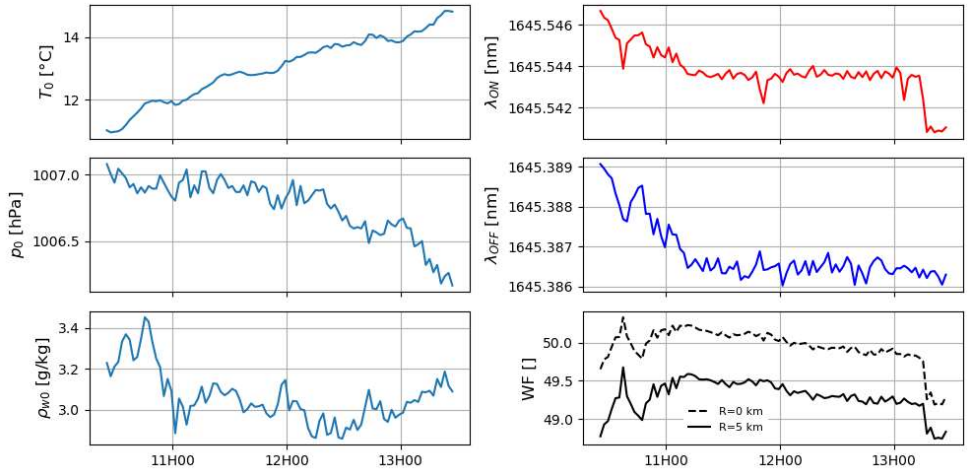

Figure 5: (Left) Time series of surface pressure, temperature, and humidity (at 50 m) provided by the SIRTA observatory. (Right) Measurements of the ON and OFF wavelengths and evolution of the weighting functions at the lidar location (R=0 km) and at a range R= 5 km.

3.2 Time series of methane mixing ratio profiles

The time series of methane mixing ratio profiles is shown in Figure 6 (left). Differential absorption coefficients are computed using linear fits applied to contiguous range gates of 10 points. As a result, the spatial resolution of the profile is reduced to 469 m. Methane mixing ratios retrieved with a 2-minute temporal resolution are subsequently averaged over 20 minutes to reduce the statistical uncertainty. The first two range gates are not shown because the corresponding measurements exhibit a substantial bias. This bias is most likely due to a difference in the overlap function between the ON and OFF laser pulses. This difference, which still needs to be investigated, may have several origins. It could arise from a difference in the pointing of the ON and OFF pulses or from a difference in transmission through the interference filter caused by larger angles of incidence during the overlap region. The measurements are compared with observations from an instrumented tower belonging to the ICOS (Integrated Carbon Observation System) network (https://meta.icos-cp.eu/resources/stations/AS_SAC), located 5 km west of the laboratory. This tower is equipped with in situ analyzers based on Cavity Ring-Down Spectroscopy (CRDS). Measurements are performed at three heights: 15 m, 60 m, and 100 m. Figure 6 (right) compares the lidar measurements at a range of 2100 m with the tower observations. The uncertainty bars of the ICOS measurements represent the dispersion of the measurements within each hourly interval. Uncertainties in the lidar measurements arise from the linear fit used to determine the differential absorption coefficient. The differences in methane concentration between the ICOS measurements (at 100 m) and the lidar measurements averaged over one hour up to a range of 3.5 km remain below 50 ppb. A fire occurred at a waste-sorting facility located in the city of Paris on the evening of April 7. This event generated an aerosol plume accompanied by an increase in atmospheric methane concentration. The methane plume was detected by the ICOS tower, with a maximum concentration observed around 08:00 local time at 15 m and around 09:00 at 60 m and 100 m. Under the nocturnally stratified atmospheric conditions, methane concentrations at 15 m reached 2500 ppb, corresponding to an increase of approximately 25%, with a measurement dispersion of 50 ppb. At 60 m and 100 m, the concentration peak was lower, around 2200 ppb. The lidar observed the tail of the plume between 10:30 and 13:30. The lidar measurements are in agreement with the tower observations within their respective errors bars and show a gradual decrease in methane concentration, indicating the end of the plume dispersion.

https://doi.org/10.5194/egusphere-2026-844
Preprint. Discussion started: 16 April 2026

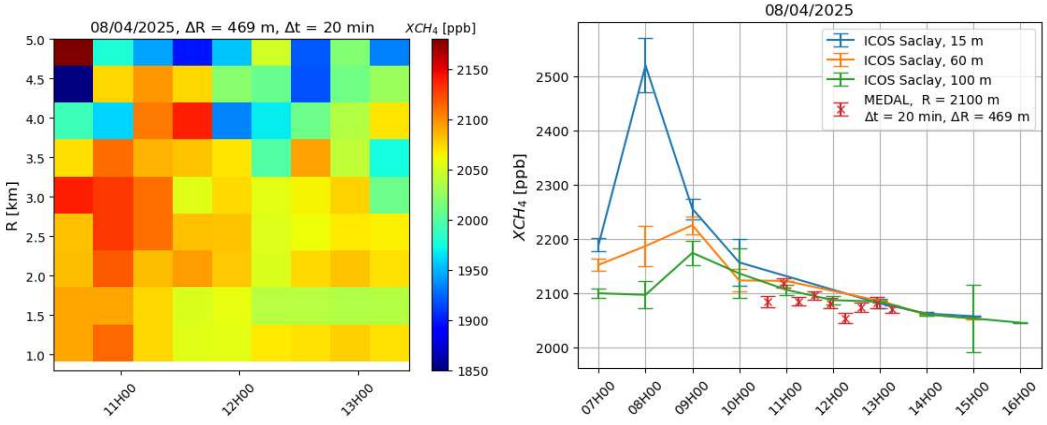

Figure 6: (Left)Time series of methane concentration profiles measured by the lidar. (Right) Comparison between ICOS tower measurements (heights: 15 m, 60 m, 100 m) and lidar measurements at a range of 2100 m.

4 Measurement error budget

4.1 Random error

From Eq. (2), the error propagation on the methane mixing ratio is given by the following expression:

$$\frac{\Delta X_{CH_4}}{X_{CH_4}} = \sqrt{\left(\frac{\Delta WF}{WF}\right)^2 + \left(\frac{\Delta\alpha}{\alpha}\right)^2} \quad (4)$$

4.1.1 Weighting function random error

The first term accounts for the error in the estimation of the weighting function arising from fluctuations of its parameters during the DIAL measurement. These parameters include temperature, atmospheric pressure, humidity, and the laser wavelength. It should be noted that temperature and pressure fluctuations affect both the dry air density and the absorption cross sections in Eq. (3). These fluctuations can be quantified using the Allan deviation computed over 2 minutes, corresponding to the temporal resolution of the DIAL measurement. The uncertainty in the weighting function associated with temperature, pressure, and wavelength variations involves absorption cross sections calculated from spectroscopic atlases. These uncertainties are therefore evaluated numerically, assuming linear error propagation for these small fluctuations. The uncertainty in the weighting function related to the water vapor mixing ratio only affects the air density and can be calculated analytically as:

$$\left.\frac{\Delta WF}{WF}\right|_{\Delta\rho_w} = \frac{\Delta\rho_w}{1+\rho_w} \approx \Delta\rho_w \quad (5)$$

Table 2 lists the 2-minute fluctuations of temperature, pressure, humidity, and the ON and OFF wavelengths, together with the associated uncertainties in the calculation of the weighting function. The uncertainties are dominated by fluctuations of the ON wavelength. Uncertainties related to the absorption cross sections depend on the wavelength positioning. As shown in Figure 7, the error induced in the weighting function by wavelength fluctuations is minimal at locations where the derivative of the absorption cross section with respect to wavelength is zero. If the ON wavelength is positioned on the flank of a methane multiplet, the relative error in the weighting function can exceed 1%.

https://doi.org/10.5194/egusphere-2026-844
Preprint. Discussion started: 16 April 2026

Table 2: Weighting function random relative errors

Parameter	Allan deviation @ 2min	WF random relative error
Temperature	0.06 K	< 0.03 %
Pressure	6 Pa	<0.005 %
Humidity	0.05 g/kg	<0.005 %
λ_{ON}	0.25 pm	<0.25 %
λ_{OFF}	0.20 pm	< 0.015 %

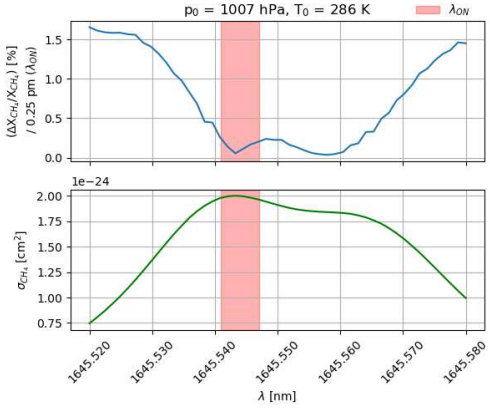

Figure 7: Relative methane mixing ratio error induced by a 0.25 pm wavelength error as a function of the ON wavelength

4.1.2 Differential absorption random error

The second term describes the error originating from the signal-to-noise ratio of the ON and OFF profiles. The uncertainty on the differential absorption coefficient corresponds to the uncertainty on the slope of the DAOD, determined using linear fits applied to each range gate. It can also be theoretically estimated from the SNR of the ON and OFF profiles (Bosenberg 1998):

$$\frac{\Delta\alpha}{\alpha} = \frac{1}{\sqrt{2}\alpha\Delta R}\sqrt{\left(\frac{1}{SNR_{ON}}\right)^2 + \left(\frac{1}{SNR_{OFF}}\right)^2} \quad (6)$$

where ΔR is the length of the range gate used to compute the differential absorption coefficient, and the signal-to-noise ratio is defined as $SNR_i = S_i/\sigma(S_i)$ at the spatio-temporal resolution of the X_{CH_4} profiles. A radiometric budget shows that the noise affecting the ON and OFF signals resulting from aerosol scattering in the boundary layer is dominated by shot noise from the signal itself and from the solar background. The SNR of the ON and OFF signals for a single laser shot can therefore be expressed as:

$$SNR_{one\ shot} = \frac{N_S}{\sqrt{N_S + N_{bkg}}} \quad (7)$$

where N_S and N_{bkg} are the numbers of detected laser and solar photons, respectively, within the detection bandwidth. The number of detected photons can be derived from the digitized voltage as:

$$N_i = \frac{S_i}{2eR_lGB} \quad (8)$$

with S_i the digitized voltage, e the electron charge, R_l the load resistance of the digitizer, G the PMT gain, and B the detection bandwidth. The SNR corresponding to the DIAL profile resolution to be used in Eq. (6) is computed assuming independent samples:

$$SNR_{DIAL} = SNR_{one\ shot}\sqrt{n_{shot}\frac{\Delta R_{DIAL}}{\Delta R_{RAW}}} \quad (9)$$

https://doi.org/10.5194/egusphere-2026-844
Preprint. Discussion started: 16 April 2026

where n_{shot} is the number of integrated laser shots required to reach the DIAL temporal resolution, ΔR_{DIAL} is the DIAL spatial resolution, and ΔR_{RAW} is the spatial resolution of the raw digitized profiles. Figure 8 shows a comparison between the theoretically calculated precision on the differential absorption coefficient derived from Eqs. (6) and the precision computed using the uncertainties of the differential absorption coefficients obtained from linear fits applied to the DIAL range gates. Both precisions exhibit a similar dependence on range but differ by approximately a factor of five. This discrepancy may originate from uncertainties in the parameters used in Eq. (8) (based on manufacturer datasheet values) and requires further investigation. The precision derived from the linear-fit uncertainties is also overestimated, as it includes the natural variability of atmospheric methane.

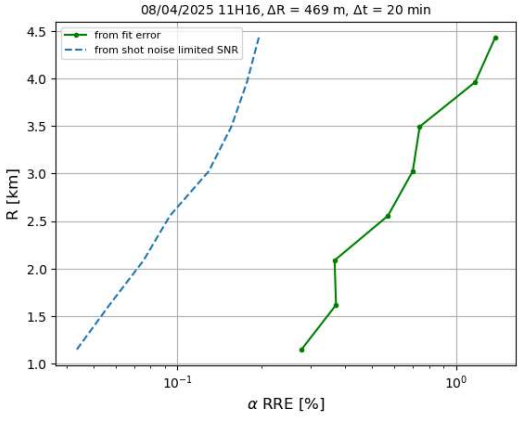

Figure 8: Comparison of relative random errors on the differential absorption coefficient derived from linear-fit uncertainties and from Eq. (6) using shot-noise-limited SNRs

4.2 Systematic error

A first source of bias arises from the accuracy of the laser spectral properties. The laser wavelength is measured using a wavemeter, whose manufacturer-specified wavelength accuracy is 0.2 ppm, corresponding to 0.3 pm at 1645 nm. This wavelength measurement uncertainty results in a 0.3% bias in the retrieved methane mixing ratio, dominated by the bias on the ON wavelength. The spectral purity of the laser was measured to be greater than or equal to 0.996, leading to a bias of 0.03% (Edouart et al. 2024). Spectroscopic data are known with a finite degree of accuracy. The R(6) multiplet of the $2\nu_3$ methane band was studied in the framework of the MERLIN mission (Delahaye et al. 2016, 2019). The methane absorption cross section for the multiplet around the ON wavelength is known to within 0.1%. For the OFF wavelength, the accuracy of the absorption cross section is 0.3%. Since the ON absorption cross section is two orders of magnitude larger than the OFF absorption cross section, the uncertainty in the spectroscopic data is dominated by the uncertainty in the ON absorption cross section.

Another source of bias is the residual differential absorption by water vapor. The ON and OFF wavelengths defined in Figure 2 are selected such that the differential absorption by water vapor is zero, thereby eliminating the corresponding bias. However, in the experimental setup used here, the laser wavelengths may experience small drifts, which can lead to residual differential water vapor absorption and introduce a bias:

$$\left.\frac{\Delta X_{CH_4}}{X_{CH_4}}\right|_{\sigma_{H_2O}} = \frac{\alpha_{H_2O}}{\alpha-\alpha_{H_2O}} \approx \frac{\alpha_{H_2O}}{\alpha} \quad (9)$$

where $\alpha_{H_2O} = n_{H_2O}(R)\left[\sigma_{H_2O}(\lambda_{ON}, R) - \sigma_{H_2O}(\lambda_{OFF}, R)\right]$ is the water vapor differential absorption, with n_{H_2O} the molecular number density of water vapor, σ_{H_2O} the water vapor absorption cross section, and α the measured differential absorption. Figure 9 (left) shows the temporal evolution of this bias during the measurement for the range gate at 2100 m. Since the slope

https://doi.org/10.5194/egusphere-2026-844
Preprint. Discussion started: 16 April 2026

of the water vapor absorption cross section is steeper around the ON wavelength, this bias is more sensitive to drifts of the ON wavelength.

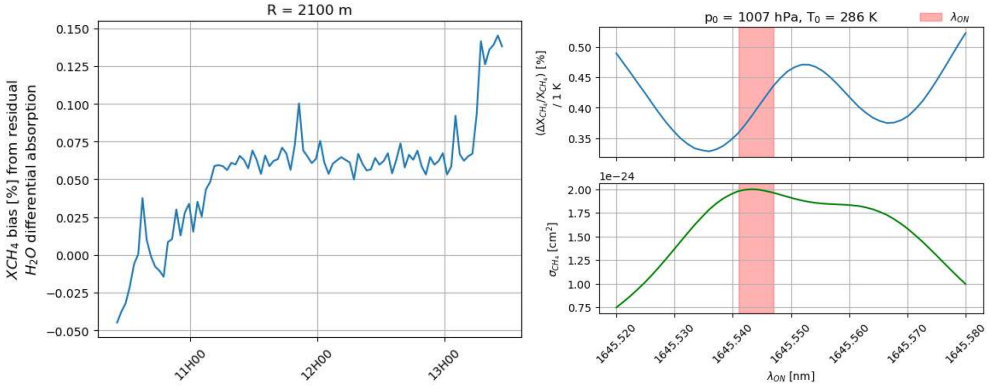

Figure 9: (left) Temporal evolution of the bias induced by residual water vapor absorption. (right) Relative methane mixing ratio error induced by a 1 K temperature profile error as a function of the ON wavelength

Table 3 summarizes the different biases and their sources. The largest instrument-related bias arises from the accuracy of the ON wavelength measurement provided by the wavemeter. The weighting function is computed using pressure, temperature, and humidity profiles. In most cases, these profiles are provided by models whose accuracy may vary. Table 3 shows that the error is highly sensitive to temperature. Figure 10 (right) illustrates the dependence of the temperature-induced error on the ON wavelength. This error is minimized near the edges of the multiplet lines and therefore does not correspond to the wavelengths for which the wavelength-induced error is minimal (see Figure 7). This type of bias may explain the slight decrease in methane concentration observed at a range of approximately 1500 m. At this distance, the laser beam passes over a valley and therefore moves significantly away from the ground surface. As a result, the temperature used in the calculation of the weighting function is likely biased, leading to a bias in the retrieved methane concentration.

Table 3: X_{CH_4} relative systematic errors

Parameter	Parameter error	X_{CH_4} systematic relative error	comment
λ_{ON}	0.2 ppm	<0.3 %	wavemeter accuracy from manufacturer
λ_{OFF}	0.2 ppm	<0.005%	wavemeter accuracy from manufacturer
Spectral purity	>0.996	<0.03%	Edouart et al. 2024
σ_{CH_4}	0.1%	<0.1%	Delahaye et al. 2016, 2019
α_{H_2O}	λ drift dependent	<0.15%	more sensitive to drifts of the ON wavelength
temperature	model dependent	<0.45 % / K	$1645.541\ nm < \lambda_{ON} < 1645.547\ nm$
pressure	model dependent	<0.07% / hPa	$1645.541\ nm < \lambda_{ON} < 1645.547\ nm$
humidity	model dependent	<0.01% / 0.1 g/kg	independent of the wavelength

4.3 Discussion

A direct comparison of the performance of this lidar with other methane DIAL measurements reported in the literature is not straightforward, as the spatio-temporal resolutions and measurement ranges vary. In addition, performance can strongly depend on atmospheric conditions, in particular aerosol loading. Nevertheless, we attempted such a comparison by using Eq. 6 to scale the different precisions reported in the literature. The relative precision of the DIAL methane measurement follows the relation:

https://doi.org/10.5194/egusphere-2026-844
Preprint. Discussion started: 16 April 2026

$$\frac{\Delta X_{CH_4}}{X_{CH_4}} \sim (\Delta R.SNR)^{-1} \quad (10)$$

Assuming that the SNR is limited by shot noise of the signal, it is proportional to the square root of the signal. Since the signal scales as $1/R^2$, the SNR ultimately varies as:

$$SNR \sim R^{-1}.(\Delta R \Delta t)^{-1/2} \quad (11)$$

As a result, the relative random precision of the methane measurement can be expressed as:

$$\frac{\Delta X_{CH_4}}{X_{CH_4}} \sim R.(\Delta R)^{-3/2}(\Delta t)^{-1/2} \quad (12)$$

This relation highlights that, for a DIAL measurement, increasing the range gate length (provided that the optical thickness allows it) is more advantageous than increasing the integration time. The above equation can be used to scale the performance measured by different lidars. Table 4 compares the performance obtained in this study with that reported in the only two publications providing a detailed evaluation of the precision of methane DIAL mixing ratio measurements.

In Stroud et al. (2023), the reported performance is slightly lower, as the laser used here is more powerful (7 W versus 0.5 W) and the telescope collecting area is also slightly larger. The performance reported in Cézard et al. (2020) is largely exceeded, since their laser power is lower (0.2 W) and the heterodyne detection scheme used is affected by significant speckle noise.

Table 4: Comparison of performance with other DIAL systems

Ref.	X_{CH_4} random relative error	R	ΔR	Δt	scaled X_{CH_4} error
This paper	0.4 %	2 km	500 m	20 min	1
Stroud et al. 2023	1-2 %	750 m	250 m	10 min	1.6-3.3
Cezard et al. 2020	100 %	150 m	30 m	30 min	60

5 Conclusion and outlook

An 1.65 µm DIAL was used to retrieve methane mixing ratio profiles within the atmospheric mixed layer along a near-horizontal line of sight (4° above the horizontal). The achieved precision reaches 0.4% at a range of 2 km with a spatio-temporal resolution of 500 m / 20 min. This level of precision made it possible to measure the late stage of the dispersion of a methane plume. These measurements were confirmed by nearby CRDS sensors.

We have shown that the main instrument-related limitation on precision is the accuracy of the ON wavelength, which depends on its position within the methane absorption line. In the configuration presented here, the laser wavelength may drift if the laser temperature is not strictly stabilized. Such drift can rapidly limit the precision of the DIAL measurement. In addition, it may induce laser instabilities (cavity mode hopping or even loss of single-mode operation), which restrict the acquisition of long, high-quality time series. To address this issue, we plan to modify the laser operating scheme by actively locking the ON seeder to the methane absorption line using a setup similar to that described in Gibert et al. 2014. This will prevent drift of the ON wavelength. The seeders will also be replaced by external-cavity diode lasers (ECDLs), which offer narrower linewidths and better spectral stability than DFB diode lasers, and are expected to improve the stability and reliability of the laser injection seeding operation. Another limiting factor is the accuracy of the DIAL retrieval due to insufficient knowledge of the temperature profile. In future measurements, we will investigate the benefit of joint observations with a Raman lidar capable of providing temperature and water vapor profiles. These lidar-derived profiles should improve the accuracy of the weighting function calculation and thereby reduce biases in the retrieved methane mixing ratio profiles.

Data availability

The data shown in this paper are available upon request.

https://doi.org/10.5194/egusphere-2026-844
Preprint. Discussion started: 16 April 2026

Author contribution

DE and FG designed the DIAL system and carried out the experimental set-up. DE performed the atmospheric measurements and the data analysis. CC contributes to the electronics of the lidar. DE prepared the manuscript with contributions from FG.

Competing interests

The authors declare that they have no conflict of interest.

Acknowledments

We thank Frédéric Nahan (Magelium/LMD) for providing the spectroscopic atlases.

Financial support

This work was supported by funding from CNRS/INSU under the 'Programme National Instrumentation Innovante Transverse'.

References

Barton-Grimley, R. A., Nehrir, A. R., Kooi, S. A., Collins, J. E., Harper, D. B., Notari, A., Lee, J., DiGangi, J. P., Choi, Y., and Davis, K. J.: Evaluation of the High Altitude Lidar Observatory (HALO) methane retrievals during the summer 2019 ACT-America campaign, Atmos. Meas. Tech., 15, 4623–4650, https://doi.org/10.5194/amt-15-4623-2022, 2022

Bösenberg, J.: Ground-based differential absorption lidar for water-vapor and temperature profiling: methodology. Appl. Opt., 37, 3845-3860, https://doi.org/10.1364/AO.37.003845, 1998

Buchwitz, M., V. V. Rozanov, and J. P. Burrows, A near-infrared optimized DOAS method for the fast global retrieval of atmospheric CH_4, CO, CO_2, H_2O, and N_2O total column amounts from SCIAMACHY Envisat-1 nadir radiances, *J. Geophys. Res.*, 105(D12), 15231–15245, doi:10.1029/2000JD900191, 2000

Butz, A., Guerlet, S., Hasekamp, O., Schepers, D., Galli, A., Aben, I., Frankenberg, C., Hartmann, J.-M., Tran, H., Kuze, A., Keppel-Aleks, G., Toon, G., Wunch, D., Wennberg, P., Deutscher, N., Griffith, D., Macatangay, R., Messerschmidt, J., Notholt, J., and Warneke, T.: Toward accurate CO2 and CH4 observations from GOSAT, Geophys. Res. Lett., 38, L14812, https://doi.org/10.1029/2011GL047888, 2011

Cezard, N., Le Mehaute, N., Le Gouët, J., Valla, M., Goular, D., Fleury, D., Planchat, C., and Dolfi-Bouteyre, A., Performance assessment of a coherent DIAL-Doppler fiber lidar at 1645 nm for remote sensing of methane and wind," Opt. Express 28, 22345-22357, https://doi.org/10.1364/OE.394553, 2020

Clerbaux, C., P. Chazette, J. Hadji-Lazaro, G. Mégie, J.-F. Müller, and S. A. Clough, Remote sensing of CO, CH_4, and O_3 using a spaceborne nadir-viewing interferometer, *J. Geophys. Res.*, 103(D15), 18999–19013, doi:10.1029/98JD01422, 1998

Delahaye, T., Maxwell, S.E., Reed, Z.D., Lin, H., Hodges, J.T., Sung, K., Devi, V., Warneke, T., Tran, H., Precise methane

https://doi.org/10.5194/egusphere-2026-844
Preprint. Discussion started: 16 April 2026

absorption measurements in the 1.64 μm spectral region for the MERLIN mission. JGR Atmos., 121, 7360–7370, doi:10.1002/2016JD025024, 2016

Delahaye, T., Ghysels, M., Hodges, J.T., Sung, K., Armante, R., Tran, H., Measurement and modeling of air-broadened methane absorption in the MERLIN spectral region at low temperatures. JGR Atmos., 124, 3556–3564, doi:10.1029/2018JD028917, 2019

Edouart, D., Gibert, F. and Cenac, C., 1.645μm Er:YAG single-mode dual-wavelength emitter for CH4 differential absorption lidar, Optics Letters, Vol. 49, No 21, https://doi.org/10.1364/OL.538254, 2024

Gibert, F., Edouart, D., Cenac, C., and le Mounier, F., 2-μm high-power multiple-frequency single-mode Q-switched Ho:YLF laser for DIAL application, Vol. 116, p. 967–976, https://doi.org/10.1007/s00340-014-5784-3, 2014

Gibert F., D. Edouart, C. Cénac, F. Le Mounier, A. Dumas: 2-μm Ho emitter-based coherent DIAL for CO2 profiling in the atmosphere, Opt. Lett., 40 (13), 3093-3096, https://doi.org/10.1364/OL.40.003093, 2015

Gibert, F., D. Edouart, P. Monnier, J. Collignan, J. Lopez: Scalar turbulent fluxes and variances in the interfacial layer from lidar observations and assessment of Lagrangian Stochastic Models. Quarterly Journal of the Royal Meteorological Society, pp.e70016. (10.1002/qj.70016), 2025

Gordon, I.E., L.S. Rothman, R.J. Hargreaves, R. Hashemi, E.V. Karlovets, F.M. Skinner, E.K. Conway, et al., The HITRAN2020 Molecular Spectroscopic Database, Journal of Quantitative Spectroscopy and Radiative Transfer ,277: 107949, https://doi.org/10.1016/j.jqsrt.2021.107949, 2022

Ikuta, K., Yoshikane N., Vasa N., Oki Y., Maeda M., Uchiumi M., Tsumura Y., Nakagawa J., and Kawada N., Jpn. J. Appl. Phys. 38 110 doi:10.1143/JJAP.38.110, 1999

Innocenti, F.; Robinson, R.; Gardiner, T.; Finlayson, A.; Connor, A. Differential Absorption Lidar (DIAL) Measurements of Landfill Methane Emissions. Remote Sens., 9, 953. https://doi.org/10.3390/rs9090953, 2017

Lorente, A., Borsdorff, T., Butz, A., Hasekamp, O., aan de Brugh, J., Schneider, A., Wu, L., Hase, F., Kivi, R., Wunch, D., Pollard, D. F., Shiomi, K., Deutscher, N. M., Velazco, V. A., Roehl, C. M., Wennberg, P. O., Warneke, T., and Landgraf, J.: Methane retrieved from TROPOMI: improvement of the data product and validation of the first 2 years of measurements, Atmos. Meas. Tech., 14, 665–684, https://doi.org/10.5194/amt-14-665-2021, 2021

Membrive, O., Crevoisier, C., Sweeney, C., Danis, F., Hertzog, A., Engel, A., Bönisch, H., and Picon, L.: AirCore-HR: a high-resolution column sampling to enhance the vertical description of CH_4 and CO_2, Atmos. Meas. Tech., 10, 2163–2181, https://doi.org/10.5194/amt-10-2163-2017, 2017.

Meng, L., Fix, A., Wirth, M., Høgstedt, L., Tidemand-Lichtenberg, P., Pedersen, C., and Rodrigo, P. J., Upconversion detector for range-resolved DIAL measurement of atmospheric CH4, Opt. Express 26, 3850-3860 https://doi.org/10.1364/OE.26.003850 2018

https://doi.org/10.5194/egusphere-2026-844
Preprint. Discussion started: 16 April 2026

Ngo, N.H., Lisak, D., Tran, H., Hartmann, J.-M., An isolated line-shape model to go beyond the Voigt profile in spectroscopic databases and radiative transfer codes. J. Quant. Spectrosc. Radiat. Transf., 129, 89–100, doi:10.1016/j.jqsrt.2013.05.034, 2013

Saunois, M., Stavert, A. R., Poulter, B., Bousquet, P., Canadell, J. G., Jackson, R. B., Raymond, P. A., Dlugokencky, E. J., Houweling, S., Patra, P. K., Ciais, P., Arora, V. K., Bastviken, D., Bergamaschi, P., Blake, D. R., Brailsford, G., Bruhwiler, L., Carlson, K. M., Carrol, M., Castaldi, S., Chandra, N., Crevoisier, C., Crill, P. M., Covey, K., Curry, C. L., Etiope, G., Frankenberg, C., Gedney, N., Hegglin, M. I., Höglund-Isaksson, L., Hugelius, G., Ishizawa, M., Ito, A., Janssens-Maenhout, G., Jensen, K. M., Joos, F., Kleinen, T., Krummel, P. B., Langenfelds, R. L., Laruelle, G. G., Liu, L., Machida, T., Maksyutov, S., McDonald, K. C., McNorton, J., Miller, P. A., Melton, J. R., Morino, I., Müller, J., Murguia-Flores, F., Naik, V., Niwa, Y., Noce, S., O'Doherty, S., Parker, R. J., Peng, C., Peng, S., Peters, G. P., Prigent, C., Prinn, R., Ramonet, M., Regnier, P., Riley, W. J., Rosentreter, J. A., Segers, A., Simpson, I. J., Shi, H., Smith, S. J., Steele, L. P., Thornton, B. F., Tian, H., Tohjima, Y., Tubiello, F. N., Tsuruta, A., Viovy, N., Voulgarakis, A., Weber, T. S., van Weele, M., van der Werf, G. R., Weiss, R. F., Worthy, D., Wunch, D., Yin, Y., Yoshida, Y., Zhang, W., Zhang, Z., Zhao, Y., Zheng, B., Zhu, Q., Zhu, Q., and Zhuang, Q.: The Global Methane Budget 2000–2017, Earth Syst. Sci. Data, 12, 1561–1623, https://doi.org/10.5194/essd-12-1561-2020, 2020.

Stroud, J.R., Wagner, G.A., Plusquellic, D.F., Multi-Frequency Differential Absorption LIDAR (DIAL) System for Aerosol and Cloud Retrievals of CO2/H2O and CH4/H2O. Remote Sens, 15, 5595. https://doi.org/10.3390/rs15235595, 2023

Veselovskii, I., Goloub, P., Hu, Q., Podvin, T., Whiteman, D. N., Korenskiy, M., and Landulfo, E.: Profiling of CH_4 background mixing ratio in the lower troposphere with Raman lidar: a feasibility experiment, Atmos. Meas. Tech., 12, 119–128, https://doi.org/10.5194/amt-12-119-2019, 2019.

Zhou, M., Langerock, B., Sha, M. K., Kumps, N., Hermans, C., Petri, C., Warneke, T., Chen, H., Metzger, J.-M., Kivi, R., Heikkinen, P., Ramonet, M., and De Mazière, M.: Retrieval of atmospheric CH_4 vertical information from ground-based FTS near-infrared spectra, Atmos. Meas. Tech., 12, 6125–6141, https://doi.org/10.5194/amt-12-6125-2019, 2019